



Nonlinear four-wave mixing with enhanced diversity and selectivity via spin and orbital angular momentum conservation

Liu, X.; Christensen, E. N.; Rottwitt, K.; Ramachandran, S.

Published in:
APL Photonics

Link to article, DOI:
[10.1063/1.5130715](https://doi.org/10.1063/1.5130715)

Publication date:
2020

Document Version
Publisher's PDF, also known as Version of record

[Link back to DTU Orbit](#)

Citation (APA):

Liu, X., Christensen, E. N., Rottwitt, K., & Ramachandran, S. (2020). Nonlinear four-wave mixing with enhanced diversity and selectivity via spin and orbital angular momentum conservation. *APL Photonics*, 5(1), [010802]. <https://doi.org/10.1063/1.5130715>

General rights

Copyright and moral rights for the publications made accessible in the public portal are retained by the authors and/or other copyright owners and it is a condition of accessing publications that users recognise and abide by the legal requirements associated with these rights.

- Users may download and print one copy of any publication from the public portal for the purpose of private study or research.
- You may not further distribute the material or use it for any profit-making activity or commercial gain
- You may freely distribute the URL identifying the publication in the public portal

If you believe that this document breaches copyright please contact us providing details, and we will remove access to the work immediately and investigate your claim.


Nonlinear four-wave mixing with enhanced diversity and selectivity via spin and orbital angular momentum conservation

Cite as: APL Photonics 5, 010802 (2020); <https://doi.org/10.1063/1.5130715>

Submitted: 07 October 2019 . Accepted: 09 December 2019 . Published Online: 10 January 2020

X. Liu, E. N. Christensen, K. Rottwitt, and S. Ramachandran

COLLECTIONS

 This paper was selected as Featured



View Online



Export Citation



CrossMark

ARTICLES YOU MAY BE INTERESTED IN

[Optical clearing and shielding with fan-shaped vortex beams](#)

APL Photonics 5, 016102 (2020); <https://doi.org/10.1063/1.5133100>

[Electro-optic eigenfrequency tuning of potassium tantalate-niobate microresonators](#)

APL Photonics 5, 016106 (2020); <https://doi.org/10.1063/1.5133029>

[Multimode nonlinear fiber optics, a spatiotemporal avenue](#)

APL Photonics 4, 110901 (2019); <https://doi.org/10.1063/1.5119434>

APL Photonics The Future Luminary Award

Journal
Impact Factor
4.383

LEARN MORE!

Nonlinear four-wave mixing with enhanced diversity and selectivity via spin and orbital angular momentum conservation



Cite as: APL Photon. 5, 010802 (2020); doi: 10.1063/1.5130715

Submitted: 7 October 2019 • Accepted: 9 December 2019 •

Published Online: 10 January 2020



X. Liu,^{1,a)} E. N. Christensen,² K. Rottwitt,² and S. Ramachandran¹

AFFILIATIONS

¹Department of Electrical and Computer Engineering, Boston University, 8 Saint Mary's St., Boston, Massachusetts 02215, USA

²Department of Photonics Engineering, Technical University of Denmark, 2800 Kgs. Lyngby, Denmark

^{a)}xlewis@bu.edu

ABSTRACT

Light that can carry orbital angular momentum (OAM) has found a variety of applications in super-resolution microscopy, optical communications, and laser machining, bringing up the need for pure OAM light generation at on-demand power levels and wavelengths. Parametric four-wave mixing is a promising platform for such source generation, and while investigations of higher-order fiber modes have revealed enhanced phase-matching possibilities, the role of the angular momentum of light in this process has not yet been substantially considered. Here, with a specially designed ring-core fiber in which over 16 OAM modes can be stably guided, we demonstrate the first experiments, to our knowledge, investigating nonlinear four wave mixing between OAM modes in an optical fiber. The large modal space as well as spin and OAM conservation rules enable a high diversity of phase matching conditions while also providing high selectivity. We report parametric wavelength translations of over 438 nm and the ability to obtain kilowatt peak-power level \sim nanosecond pulses of pure OAM beams at user defined colors.

© 2020 Author(s). All article content, except where otherwise noted, is licensed under a Creative Commons Attribution (CC BY) license (<http://creativecommons.org/licenses/by/4.0/>). <https://doi.org/10.1063/1.5130715>

I. INTRODUCTION

Light fields with helical phase fronts in the form of $\exp(\pm iL\phi)$ have been shown to carry orbital angular momentum (OAM).^{1,2} This has attracted a lot of attention for potential applications in a wide range of fields such as nanoscale microscopy,^{3,4} optical tweezers,⁵ laser machining,⁶ and communications in the classical⁷ and quantum⁸ regimes. In most, if not all, of these cases, there are needs for generating power-scalable pure OAM beams at on-demand wavelengths. The primary means of achieving this has been intracavity^{9,10} or extracavity^{11,12} mode conversion of a conventional laser or parametric oscillator source. Such techniques necessarily require mode converters that are, themselves, wavelength-diverse and power scalable. Bulk $\chi^{(2)}$ and $\chi^{(3)}$ nonlinearities have also been exploited,^{13,14} but the short interaction lengths have thus far prevented these techniques from being power scalable. A recent alternative approach is the generation of a supercontinuum¹⁵ in an OAM fiber, but this yields new colors at only the same OAM mode order as that of the original pump. In addition, as with most

supercontinuum sources, this approach yields low power-spectral densities and is most suitable primarily for ultrashort pulses.

Here, we report the first, to the best of our knowledge, demonstration of four-wave mixing (FWM) amongst fiber modes that stably carry OAM and hence demonstrate power-scalable wavelength-diverse OAM generation. As a subset of higher order fiber modes (HOMs), OAM modes retain the inherent advantages of a multimode system—that of a dramatically enhanced degree of freedom for phase matching arising from the plethora of available modes.^{16–18} The presence of angular momentum, as we will show, results in additional constraints that improve the selectivity of this multimode platform while also providing for more efficient interactions.

II. THE OAM-FWM PLATFORM

The parametric process of FWM enables new frequency generation when energy and momentum conservation conditions are simultaneously satisfied. For a conventional mono-mode FWM

process, where all the interacting waves are in the same transverse spatial mode, the phase matching condition is governed by the second and fourth order dispersion terms.¹⁹ As a general rule, when the pump beam is at a wavelength at which it experiences anomalous dispersion, broadband gain close to the pump wavelength is obtained—a process also referred to as modulation instability (MI). In contrast, narrow gain peaks that are substantially spectrally separated from the pump wavelength are obtained when the pump experiences normal dispersion. In the case of intermodal FWM, these simple dependencies on dispersion no longer hold, and the phase matching condition, ignoring the correction due to self-phase and cross-phase modulation, is given by¹⁶

$$\Delta\beta = \frac{n_{\text{eff}}^j(\lambda_p)}{\lambda_p} + \frac{n_{\text{eff}}^k(\lambda_q)}{\lambda_q} - \frac{n_{\text{eff}}^l(\lambda_s)}{\lambda_s} - \frac{n_{\text{eff}}^m(\lambda_{\text{as}})}{\lambda_{\text{as}}} = 0, \quad (1)$$

where $\Delta\beta$ is the total mismatch between propagation constants that must be minimized, the subscript “p,” “q,” “s,” and “as” represent the two pumps, Stokes, and anti-Stokes waves, respectively, with corresponding mode order denoted by the superscripts “j” through “m.” It is then trivial to show that phase matching is automatically satisfied when the four photons lie on a straight line of a n_{eff} vs λ plot. Thus, more available spatial modes increase the degrees of freedom with which to obtain desired FWM interactions. In addition, FWM with spatial modes that stably (linearly) propagate in an optical fiber enables maximizing the lengths over which the nonlinear interaction remains coherent, yielding power-scalable parametric wavelength conversion.²⁰ All of the above is true for any multimode system, and we now describe the unique aspects of cases where these modes additionally carry angular momentum.

The normalized transverse electric fields of OAM fiber modes are given by²¹

$$E(r, \phi) = F(r) \begin{Bmatrix} \sigma^{\pm} e^{\pm iL\phi} \\ \sigma^{\pm} e^{\mp iL\phi} \end{Bmatrix} \begin{pmatrix} \text{SOa} \\ \text{SOaa} \end{pmatrix}, \quad (2)$$

where $F(r)$ is the normalized radial field distribution and ϕ denotes the azimuthal angle. L is the topological charge, associated with $\pm L\hbar$ OAM per photon, and σ^{\pm} denote the left and right circular polarizations, corresponding to $\pm\hbar$ of spin angular momentum (SAM) per photon (\hbar is reduced Planck’s constant). Hence, spin-orbital aligned (SOa) modes carry OAM and SAM of the same sign, while spin-orbital antialigned (SOaa) modes have OAM and SAM of opposite signs.

The polarization dependence of $\chi^{(3)}$ nonlinearities demands that SAM be independently conserved.²² In addition, the strength of any FWM interaction is proportional to a field overlap integral, which, for OAM modes, is given by

$$f_{j,k,l,m} = \int F_j(r) F_k(r) F_l(r) F_m(r) r dr e^{i(\Delta L)\phi} d\phi, \quad (3)$$

$$\Delta L = -L_j - L_k + L_l + L_m, \quad (4)$$

where the subscripts follow the same definitions as above and ΔL is the OAM mismatch between the four interacting waves. The overlap integrals of Eqs. (3) and (4) point to some interesting and beneficial differences. First, this integral is nonzero and hence FWM occurs only when OAM is conserved across the modes, that is, when

$\Delta L = 0$. This provides a higher degree of selectivity compared to conventional HOMs and reduces the possibility of parasitic FWM processes competing with a desired process. Second, as we will show below, OAM modes in fibers designed to stably propagate them differ primarily in phase and not amplitude, that is, their intensity profiles are similarly ring-shaped across mode order L . Thus, the overlap integral of Eq. (3) is maximized for OAM modes, making it more efficient than conventional HOM-FWM.

Here, we present three manifestations of FWM with modes that carry OAM, differing primarily in the superposition of OAM and SAM values for the pump mode: (a) degenerate OAM and SAM pump, which leads to traditional MI-like FWM close to the pump wavelength; (b) degenerate OAM but nondegenerate SAM values for the pump, leading to polarization diverse parametric generation; and (c) degenerate SAM but nondegenerate OAM values for the pump, leading to wideband, OAM diverse parametric generation.

III. EXPERIMENTAL SETUP

The experiment setup is shown in Fig. 1(a). The pump laser is a Yb-doped fiber amplifier seeded by a Nd:YAG microchip laser (Teem Photonics SNP-20F-100) that produces 0.6-ns pulses at a repetition rate of 19.5 kHz. The Yb-doped fiber amplifier comprises a 1.5-m-long polarization maintaining gain fiber (Nufern PLMA-YDF-25/250-VIII), yielding peak powers of up to 120 kW—substantially more than that required in our experiments, in which the input powers were controlled by an attenuator comprising a half-wave plate (Thorlabs WPH05M-1064) and polarization beam splitter (Thorlabs CM1-PBS253).

A spatial light modulator (Hamamatsu LCOS-SLM $\times 10468-08$) coded with a spiral phase plate is used to convert the Gaussian beam from our source into an OAM state with the desired topological charge in the far field. A quarter wave plate (Thorlabs WPQ05M-1064) that follows enables the desired OAM/SAM combinations—either the SOa or SOaa states or their superpositions—to be input into our test fiber.

The seed arm was built with a Ti:sapphire laser (Spectra-Physics, Model 3900S) tuned to 888.8 nm; the mode excitation setup is similar to that of the pump arm except that another half wave plate (Thorlabs WPH05M-1064) and quarter wave plate (Thorlabs WPQ05M-808) are used to compensate for the polarization scrambling from the dichroic mirror and the wavelength mismatch of the seed light with QWP2.

The fiber under test features an air core surrounded by a high-index ring that has been previously shown to facilitate stable guidance of OAM modes over km lengths.²³ Figure 1(b) shows the refractive index profile of this fiber. Simulations suggest that single-radial order OAM modes of $|L| = 8, 9, 11$, and 12 are stably guided at the pump wavelength of 1064 nm (the $L = 10$ mode is not stable due to an accidental degeneracy with other radial mode orders but is stable at other wavelengths, such as 1030 nm). The length of fiber used in experiments described in Secs. IV A–IV C is 1.5 m, which was cut back to 0.9 m for the experiments described in Sec. IV D. At the output of the air core fiber [see Fig. 1(a)], a camera (Thorlabs DCC1645C for 600–1100 nm and Allied Vision Technologies “Goldeye” for 1100–1500 nm), a free space large-area InGaAs 5-GHz detector (DET08C), an oscilloscope (Agilent 86100A), and an optical spectrum analyzer (OSA—Ando AQ6317) are used to characterize

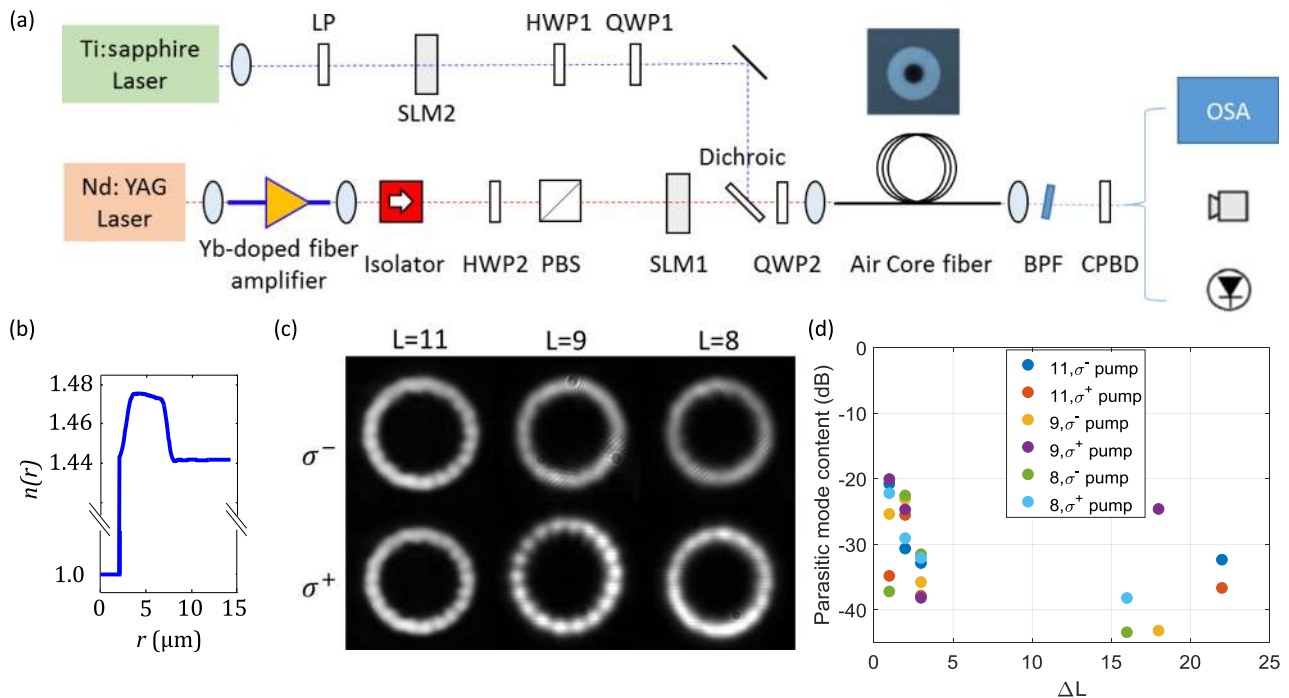


FIG. 1. (a) Experiment setup—LP: linear polarizer, PBS: polarization beam splitter, HWP: half wave plate, QWP: quarter wave plate, SLM: spatial light modulator, OSA: optical spectrum analyzer, BPF: bandpass filter, CPBD: circular polarizing beam displacer, fiber facet image shown in the inset. (b) The measured refractive index profile of the OAM fiber used for the experiments. (c) Images of modes used in our experiment. (d) Mode content analysis by ring technique.

the mode image and purity, as well as its behavior in the temporal and frequency domains at all relevant wavelengths by employing bandpass filters (BPFs) to selectively interrogate different spectral components. A 200- μm core multimode fiber (Thorlabs FG200LEA) is used for coupling light from all the modes into the OSA. In addition, imaging the output with a tilted lens and circular polarization beam displacer (CPBD) in the beam path allows measuring the OAM and SAM of the output beams. This is because the polarization projection ratios reveal SAM, and the number and orientation of fringes when the output is projected in the far field off a tilted lens reveals the OAM order.²⁴

Figure 1(c) shows representative images of the beam at the output facet of the fiber for different input OAM and SAM orders at the pump wavelength of 1064 nm with $\sim 45\%$ – 50% coupling efficiency. We use spatial interferometry²⁵ to measure mode purity; Fig. 1(d) shows the relative powers of each parasitic mode, denoted by the difference of its topological charge in relation to the charge L of the desired beam. In all cases, the mode purity was >20 dB.

IV. RESULTS

A. Degenerate OAM and SAM pump

When the input pump light is in a single OAM and SAM state, the system is effectively single-moded although the fiber is itself multimoded. Such monomode systems would follow the same rules as for traditional single mode systems described in Sec. II. Hence, anomalous dispersion at the pump wavelength would lead to MI,

which is a manifestation of FWM leading to broadband emission close to the pump wavelength.

We confirm these expectations by individually pumping in the $L = +9$; σ^+ and $L = +11$; σ^+ modes of the fiber with peak powers of 8.3 kW and 6.5 kW, respectively. Both modes have anomalous dispersion ($\sim 50 \text{ ps km}^{-1} \text{ nm}^{-1}$ and $\sim 72 \text{ ps km}^{-1} \text{ nm}^{-1}$, respectively) at the pump wavelength of 1064 nm [Fig. 2(a) shows the simulated dispersion vs λ for these two modes]. The corresponding spontaneous FWM spectra are shown in Fig. 2(b).

Note that increasing pump mode order shifts the Stokes and anti-Stokes emission wavelengths toward the pump, and the bandwidth decreases as well. This is consistent with single mode FWM, where the peak emission wavelengths move closer to the pump, and emission bandwidths decrease, as the magnitude of anomalous dispersion at the pump wavelength increases. These spectral characteristics suggest that the entire emission in either of these experiments would have been in the same mode as the pump. Filtering out representative spectral components (1064 nm for pump and peak emission wavelengths, 1053 nm and 1076 nm for the anti-Stokes and Stokes with $L = +9$; σ^+ pump, respectively, 1055 nm and 1074 nm for the anti-Stokes and Stokes with $L = +11$; σ^+ pump) allows measurement of their mode content via the tilted lens technique mentioned in Sec. III. We find that all spectral features remain in the same OAM mode as that of the original pump mode, and polarization purity remains greater than 20 dB. Hence, these experiments confirm that FWM with single OAM states behave identically to single-mode FWM, with the added flexibility

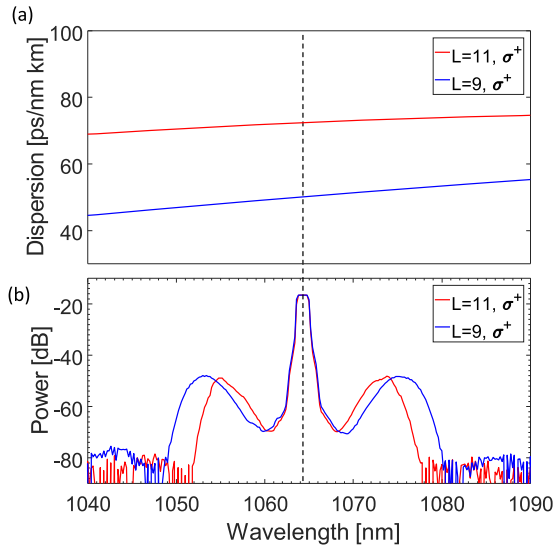


FIG. 2. (a) Simulated dispersion curve for $L = +9, \sigma^+$ and $L = +11, \sigma^+$. (b) Spontaneous FWM spectrum with either $L = +9, \sigma^+$ or $L = +11, \sigma^+$ pump.

of tuning dispersion by mode order rather than waveguide design alone.

B. Degenerate OAM; nondegenerate SAM pump

Substantially distinct nonlinear behavior occurs simply by changing the pump mode from an OAM-SAM singlet state to a pump with the same OAM but with linear polarization. As the description of fiber OAM modes in Sec. II conveys, OAM fiber eigenmodes are either SOa or SOaa. Thus, a linear— \hat{x} —polarization implies that the pump is now equipartitioned into two modes with different n_{eff} (in our air core fibers, this difference is $\sim 10^{-4}$). The dynamics of this intermodal process are better visualized with Fig. 3(a), which is a plot of the simulated n_{eff} vs λ for the pump and a few neighboring OAM modes. The blue and orange curves represent the n_{eff} distributions of the $L = +11; \sigma^+$ (SOa) and σ^- (SOaa) modes, respectively—these are the pump modes used in our experiment. Also shown (in purple and dark green) are n_{eff} s of the $L = +10; \sigma^+$ and $L = +12; \sigma^-$ modes, respectively. The two pump modes, being spectrally degenerate, have an average n_{eff} given by the midpoint between their respective n_{eff} vs λ curves [apparent in the zoomed-in inset of Fig. 3(a)]. These simulated curves enable prediction of the possible FWM pathways in the system. SAM conservation requires that, since the pump modes are split into σ^+ and σ^- polarizations, the Stokes and anti-Stokes lines must also carry SAM of opposite signs,

$$\sigma_{\text{anti-Stokes}}^{\pm} \leftarrow \sigma_{\text{pump}}^{+} + \sigma_{\text{pump}}^{-} \rightarrow \sigma_{\text{Stokes}}^{\mp}. \quad (5)$$

The two possible pathways given the above constraint are represented by straight dashed lines in the n_{eff} vs λ curves of Fig. 3(a), recall, from Sec. II that intermodal processes represent straight lines in n_{eff} vs λ when energy conservation of the four photons is assured.

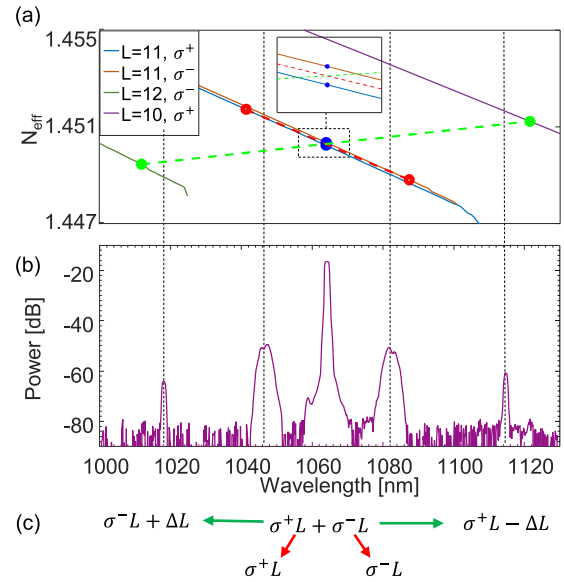


FIG. 3. (a) Simulated effective refractive index curves for different modes, the inset figure shows the zoom-in refractive index of the two nondegenerate states $L = +11, \sigma^{\pm}$, the red and green dashed lines represent for two phase matching curves. (b) Spontaneous FWM spectrum with $L = +11; \hat{x}$ pump at 1064 nm. (c) Symbolic representation of each nonlinear product with experimentally verified OAM and SAM for every peak, the arrows denote different processes.

The red dashed line conserves OAM trivially, as in case A (degenerate SAM and OAM) but predicts Stokes (at 1082 nm) and anti-Stokes (1047 nm) emission in the σ^- and σ^+ polarization state, respectively. Figure 3(b) shows experimentally measured spectra with 6.5 kW pump peak power—the excellent match with theoretical predictions is borne out not only by the spectral coincidence between the theory and experiment but also by the fact that modal content measurements at the Stokes and anti-Stokes wavelengths (using a CPBD and tilted lens) reveal exactly the same OAM and SAM content as predicted. Measured polarization extinction ratios for both modes were greater than 14 dB.

The second (green) dashed line in Fig. 3(a) predicts the alternative FWM pathway. Here, the polarization of the Stokes and anti-Stokes light flips compared to the first pathway as indicated in Fig. 3(c) but still yields SAM conservation according to Eq. (5). The participation of different mode orders also requires nontrivial OAM conservation, represented by the pathway,

$$12^{(as)} \leftarrow 11^{(p)} + 11^{(q)} \rightarrow 10^{(s)}. \quad (6)$$

Given that intermodal n_{eff} differences are an order of magnitude larger than the n_{eff} differences between SOa and SOaa modes of the same $|L|$, the wavelength separation with respect to the pump at which FWM products appear is also larger, and the large slope difference between the phase matching and n_{eff} curves predicts a much smaller bandwidth. The spectrum in Fig. 3(b) bears this out, with distinct and narrower emissions at 1015 nm and 1118 nm, respectively. These wavelengths do not match the predictions as well as the intramodal FWM case described earlier in this section [see dashed black lines showing correspondences between the simulations of

Fig. 3(a) and experimental features in Fig. 3(b)]. This discrepancy may arise from the fact that simulations of n_{eff} 's across modes may be less accurate than those for a single mode. To confirm that the observed pathway is the same as prediction, we also carried our SAM and OAM content measurements using the CPBD and tilted lens technique described earlier. We find that the anti-Stokes emission is in the $L = +12; \sigma^-$ mode and the Stokes emission is in the $L = +10; \sigma^+$ mode, precisely as predicted by Eq. (6). Moreover, we measure polarization purity of each of these emissions to be greater than 16 dB, indicating a controlled and exclusive FWM process, as predicted by simulations.

Finally, we note that the strengths of emissions for the two distinct pathways are not similar. Using simulated field profiles and Eq. (3), we find that the overlap integral for the monomode pathway (red dashed line) is $8.76 \times 10^{-3} \mu\text{m}^{-2}$ and that for the other pathway (green dashed line) is $4.08 \times 10^{-3} \mu\text{m}^{-2}$. The different overlap integrals and their relative magnitudes qualitatively match with the experiment, which indicates that the degenerate OAM pathway would be more efficient than the nondegenerate OAM pathway of Eq. (6).

C. Degenerate SAM; nondegenerate OAM pump

The last configuration we consider involves the pump modes sharing the same SAM state σ^- , which, due to SAM conservation, implies, as in the first case A (pump with degenerate SAM and OAM), that all nonlinear products would also have the same polarization σ^- . We consider an input pump comprising equal powers in the $L = +8; \sigma^-$ and $L = +9; \sigma^-$ modes, the phase matching

relationships of which are depicted in Fig. 4(a) with solid curves representing, as before, n_{eff} vs λ for each mode.

Multiple FWM pairs are expected since the pump modes now have vastly different n_{eff} . As with the analysis of nondegenerate SAM pump (case B), the equivalent n_{eff} for the pumps lies at the average of the n_{eff} vs λ curves for the $L = +8; \sigma^-$ and $L = +9; \sigma^-$ modes at 1064 nm, resulting in three distinct phase matching pathways (shown by the dashed lines). The red dashed line intersects with the $L = +9; \sigma^-$ and $L = +8; \sigma^-$ n_{eff} curves and creates a photon pair at 888.8 nm and 1326 nm; the green dashed line yields $L = +11; \sigma^-$ and $L = +6; \sigma^-$ photon pairs at 937.4 nm and 1231 nm, and finally, the orange dashed line gives rise to $L = +10; \sigma^-$ and $L = +7; \sigma^-$ photon pairs at 991.5 nm and 1149 nm,

$$9^{(888.8 \text{ nm})} \leftarrow 8^{(1064 \text{ nm})} + 9^{(1064 \text{ nm})} \rightarrow 8^{(1326 \text{ nm})}, \quad (7)$$

$$11^{(937.4 \text{ nm})} \leftarrow 8^{(1064 \text{ nm})} + 9^{(1064 \text{ nm})} \rightarrow 6^{(1231 \text{ nm})}, \quad (8)$$

$$10^{(991.5 \text{ nm})} \leftarrow 8^{(1064 \text{ nm})} + 9^{(1064 \text{ nm})} \rightarrow 7^{(1149 \text{ nm})}. \quad (9)$$

Performing the experiment required a setup slightly modified in comparison to the generic configuration shown in Fig. 1(a). Since we need to excite two distinct pump mode orders, the incoming pump light from the amplified Nd:YAG laser was split on to two distinct spatial patterns on SLM1, which were then recombined with a 3-dB coupler. Figure 4(b) shows the experimentally measured spectrum for this condition with 6.7 kW peak power in each pump mode. As the black dashed lines showing correspondence between the simulated crossing points in Fig. 4(a) and peaks of the spectral features

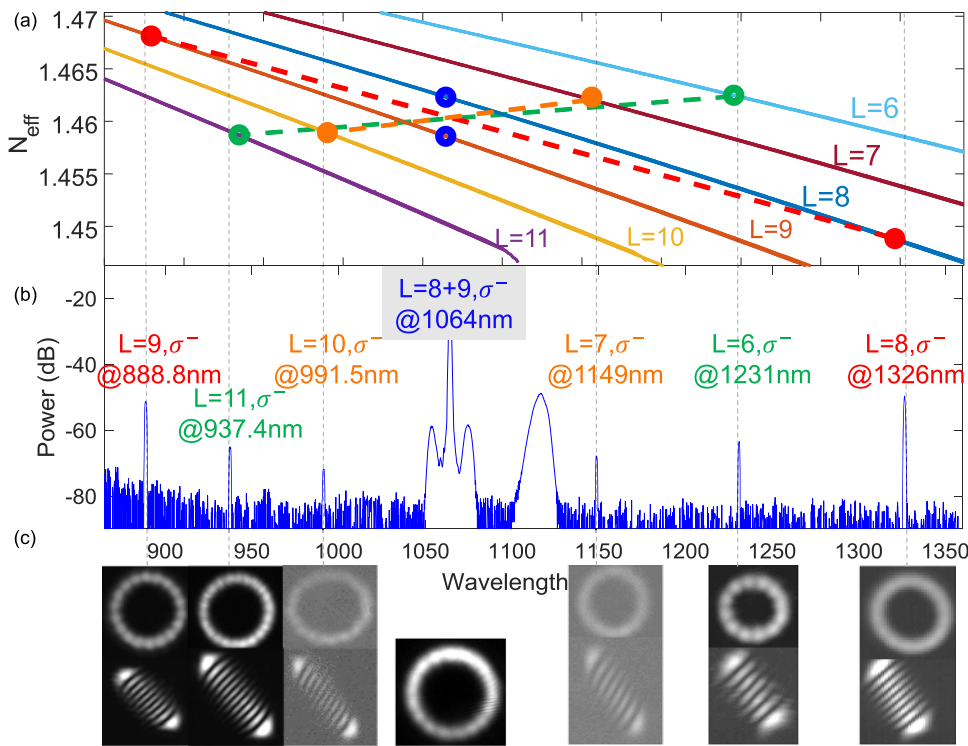


FIG. 4. (a) Simulated effective refractive index curve for different modes and phase matching curves. (b) Spontaneous FWM spectrum with a combined $L = +8; \sigma^-$ and $L = +9; \sigma^-$ pump, bandwidths of the 888.8 nm, 937.4 nm, and 991.5 nm peaks: 230 GHz, 68 GHz, and 152 GHz, respectively. (c) Mode images (top) and tilted lens image (bottom) for every peak.

in Fig. 4(b) indicate, an excellent match between theory and experiment is obtained. We also measure output images [Fig. 4(c)]. The top row shows mode images at the output of the fiber after spectral isolation with appropriate spectral filters. The bottom row shows images after the output passes through a CPBD, hence selecting only the σ^- polarization, and a tilted lens, which reveals the OAM content in the form of fringes whose number equals the $|L|$ value of the mode as well as sign of OAM (top-down diagonal for $+L$ and bottom-up diagonal for $-L$ modes).

We confirm that the experimentally deduced OAM and SAM content of each of these modes matches the predictions of Eqs. (7)–(9) and, along with the excellent spectral matches of the various FWM emissions, provides a high degree of confidence that the OAM-FWM platform indeed provides the multitude of degrees of freedom as predicted.

Note that, at the pump wavelength, the output mode image does not look as cylindrically symmetric as those at the Stokes and anti-Stokes lines. This apparent degradation is, in fact, expected since the pump comprises two modes $L = +8; \sigma^-$ and $L = +9; \sigma^-$, respectively, and their coherent interference would indeed lead to the representative “heavy-side” circular image, as shown. A corresponding tilted lens image for the pump is not shown because this technique, which counts fringes, works well only when a single L value exists—instead, we independently confirmed pure mode excitation at the pump wavelength by doing similar measurements for each pump mode path at low power, when only linear transmission occurs.

We calculate the field overlap integral—Eq. (3)—of the three different pathways to compare with the experimentally observed strengths:

Table I indicates a discrepancy between theoretically predicted efficiencies and experimentally observed spectral powers. The $L = +10; \sigma^-$ and $L = +7; \sigma^-$ pair, whose overlap integral is equal to 6.93×10^{-3} , which should correspond to ~ 14 dB higher efficiency than the $L = +11; \sigma^-$ and $L = +6; \sigma^-$ pair whose overlap integral is 6.78×10^{-3} but, in fact, has the least power. This likely arises from the fact that either the $L = +10; \sigma^-$ mode at 991.5 nm or the $L = +7; \sigma^-$ at 1149 nm is linearly unstable. Previous characterizations of linear properties of OAM modes in our air core fiber have revealed that different OAM modes at specific, small wavelength ranges can suddenly become unstable because they correspond with wavelengths at which higher radial order parasitic modes are exactly phase matched. The use of OAM fibers typically entails designing the fiber to avoid such crossings in the wavelengths of interest. A linearly unstable mode would be unable to build up the nonlinear phase, thereby rendering any FWM process in which it participates inefficient. Additional tests on mode stability need to be performed

to confirm this hypothesis for the origin of low efficiency for this case.

Finally, note the two other spectral features not predicted by the FWM pathways (dashed lines) of Fig. 4(a). We surmise that the broad band peak at 1120 nm is Raman scattering from the pump modes. This hypothesis is supported by the fact that it is 13 THz away from the pump wavelength, which corresponds to a Raman Stokes shift, and also because its measured SAM state is the same as the pump (σ^-), as expected for Raman scattering.²⁶ We were, however, unable to fully confirm this hypothesis by also measuring OAM content because the interferometric and tilted lens mode projection techniques we used to measure OAM content of other lines only work for single OAM states, and Raman, being a self-phase matched process, would be expected to have the same (mixed) mode content of the pump. The other feature is close to the pump peaking at 1051 nm and 1079 nm, respectively. We found that their mode content varied between $L = +8; \sigma^-$ and $L = +9; \sigma^-$ depending on the power ratio of the $L = +8; \sigma^-$ and $L = +9; \sigma^-$ content of the input pump. Hence, these are simply MI peaks arising from pump photons in each individual pump mode.

D. Power scaling

With various possible phase matching conditions on hand, the next question we want to address is whether we can build a power-scalable laser based on the OAM-FWM process, which demands that such processes be coherent and robust—a requirement potentially satisfied by OAM fiber modes, given their inherent linear stability with respect to modal as well as polarization perturbations. We test this with seeded FWM experiments so that parametric gain, power-scaling, etc., may be quantitatively assessed. The pump is a superposition of the $L = +8; \sigma^-$ and $L = +9; \sigma^-$ modes (as in case C) with a total peak power level of ~ 10 kW entering the fiber sample at 1064 nm; the corresponding spectrum with pump alone is shown in Fig. 5(a). Since the spectra of Fig. 4(b) indicates that the FWM pathway yielding Stokes at 1326 nm in the $L = +8; \sigma^-$ mode and anti-Stokes at 888.8 nm in the $L = +9; \sigma^-$ mode is most efficient, we seed the anti-Stokes arm with 10 mW of power in the $L = +9; \sigma^-$ mode. The spectrum of the seed laser is shown in Fig. 5(b). The resultant spectrum with both pump and seed present is shown in Fig. 5(c). The seed light experienced 51 dB of intrapulse gain, calculated based on the on-off gain at the seed wavelength and repetition rate of the pump laser. This large gain is indicative of a robust, coherent FWM process. The insets of Figs. 5(b) and 5(c) also show the corresponding output mode images as well as beam projections through a tilted lens. Note that the amplified FWM products at both the Stokes and anti-Stokes lines appear to be of much higher mode purity than the input seed—this is consistent with the fact that the high selectivity of OAM-FWM processes ensures parametric amplification for only the phase-matched mode.

Figure 5(d) shows the temporal profile of the measured pump pulse with (red line) and without (blue line) the seed. The center of the pump pulse has a maximum instantaneous depletion of $\sim 63\%$, and the overall pump depletion is 29%. This large pump depletion also accounts for the spectral suppression of parasitic nonlinear products shown in Fig. 5(c). The temporal profiles of the anti-Stokes and Stokes pulses are shown in Figs. 5(e) and 5(f), respectively, revealing an anti-Stokes pulse peak power of ~ 2.8 kW

TABLE I. Overlap integral and relative spectral power for all nonlinear products.

Nonlinear process	Overlap integral (μm^{-2})	Relative spectral power (dB)
$10^{\text{as}} \leftarrow 8^{\text{p}} + 9^{\text{q}} \rightarrow 7^{\text{s}}$	6.93×10^{-3}	−62
$11^{\text{as}} \leftarrow 8^{\text{p}} + 9^{\text{q}} \rightarrow 6^{\text{s}}$	6.78×10^{-3}	−57
$9^{\text{as}} \leftarrow 8^{\text{p}} + 9^{\text{q}} \rightarrow 8^{\text{s}}$	6.92×10^{-3}	−43

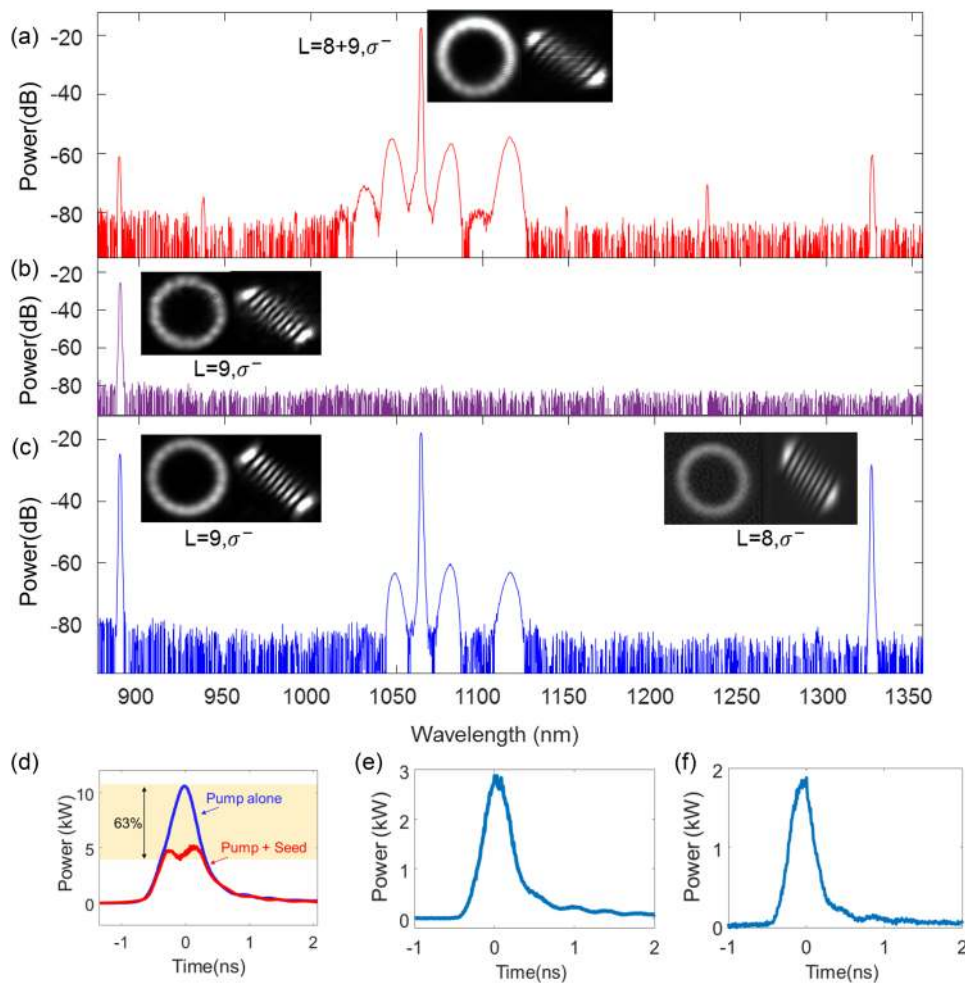


FIG. 5. (a) Spontaneous FWM spectrum with a combined $L = 8; \sigma^-$ and $L = 9; \sigma^-$ pump at 1064 nm. (b) Seed laser spectrum (Ti:sapphire laser). (c) Spectrum with both pump and seed light on. (d) Pump pulses with and without seed on. (e) Anti-Stokes light pulse. (f) Stokes light pulse.

and a Stokes pulse peak power of ~ 1.85 kW. The ratio of these powers is identical to that of the inverse ratio of their respective wavelengths, indicating that photon number is conserved in this process, as expected of any robust FWM process. The resultant FWM products have pulse widths of 356 ps for the Stokes line and 390 ps for the anti-Stokes line—shorter than the 650 ps of the pump, consistent with the fact that nonlinear temporal shaping tends to reduce pulse widths.

When optimizing the experimental parameters to obtain the above results, we found that the overall efficiency increased as fiber lengths were shortened. This is reminiscent of early FWM experiments with photonic crystal fibers (PCFs),²⁷ which found that fiber diameter fluctuations modulate the phase matching wavelength along the fiber length, leading to broadening of FWM lines and an attendant reduction in efficiency. Shorter lengths than the 0.9-m we used in our experiments would likely have resulted in even higher efficiency than the $\sim 63\%$ peak depletion we measured, but we were unable to test this hypothesis due to limitations in available pump power. More importantly, just as FWM efficiencies improved with manufacturing improvements in PCFs, we expect that future

manufacturing optimization of OAM fibers would improve efficiencies for OAM-FWM processes too. Finally, note that we used Q-Switched pump pulses for our experiments, which is why the overall efficiency was vastly different from the instantaneous peak efficiency. Optimal rectangular pump pulses would potentially yield overall efficiencies as high of the measured peak efficiency of 63%.

V. SUMMARY, CONCLUSIONS, AND OUTLOOK

We have demonstrated the first four-wave mixing experiments with fiber modes that can carry orbital angular momentum. OAM modes, being a subset of modes in a multimode fiber, retain several of the advantages that have been recently discussed in the emerging field of multimode nonlinear optics, namely, phase-matching diversity. In addition, they provide higher selectivity that enables avoiding undesired nonlinear pathways in favor of the desired processes. This has often been a problem in attempts at using multimode fibers for controllable nonlinear interactions because the modes of conventional fibers typically mix, hence reducing coherence of the

nonlinear process. OAM fiber modes offer two major advantages in this regard: (1) they are the only known set of fiber modes, to date, that can transmit for km-lengths without mode mixing, hence providing for a very robust and stable platform in which to exploit the multimodality of such fibers; and (2) angular momentum conservation rules result in distinct, specific, and hence tailorable selection rules, enabling isolating and obtaining *specific* nonlinear products, at user-defined wavelengths and powers.

The attributes illustrated in our experiments (wavelength-translation ranges exceeding 400 nm, peak powers exceeding kW, wavelength ranges unconstrained by material dispersion) suggest that OAM fiber modes are an attractive alternative to dispersion-tailored single mode fibers (such as PCFs) for a variety of power-scalable nonlinear optics applications. In addition, given the immense current interest in free-space OAM beams, FWM with OAM fibers could also become the source generation and mode conversion methods of choice for applications where current options are constrained by the need for (often lossy) mode converters at nonstandard wavelengths.

ACKNOWLEDGMENTS

The authors would like to thank P. Kristensen (OFS-Fitel LLC) for manufacturing the air core fibers used in the experiment. This work was supported by the Vannevar Bush Faculty Fellowship (Grant No. N00014-19-1-2632), the Air Force Office of Scientific Research (AFOSR) BRI program (Grant No. FA9550-14-1-0165), the Office of Naval Research (ONR) (Grant No. N00014-17-1-2519), Brookhaven National Labs (Contract No. 354281), and Danish council for independent research (Grant No. DFF 4184-00433).

REFERENCES

- ¹L. Allen *et al.*, "Orbital angular momentum of light and the transformation of Laguerre-Gaussian laser modes," *Phys. Rev. A* **45**(11), 8185 (1992).
- ²A. M. Yao and M. J. Padgett, "Orbital angular momentum: Origins, behavior and applications," *Adv. Opt. Photonics* **3**, 161–204 (2011).
- ³T. A. Klar, E. Engel, and S. W. Hell, "Breaking Abbe's diffraction resolution limit in fluorescence microscopy with stimulated emission depletion beams of various shapes," *Phys. Rev. E* **64**, 066613 (2001).
- ⁴L. Yan *et al.*, "Q-plate enabled spectrally diverse orbital-angular-momentum conversion for stimulated emission depletion microscopy," *Optica* **2**(10), 900–903 (2015).
- ⁵M. Padgett and R. Bowman, "Tweezers with a twist," *Nat. Photonics* **5**(6), 343 (2011).
- ⁶A. V. Nesterov and V. G. Niziev, "Laser beams with axially symmetric polarization," *J. Phys. D: Appl. Phys.* **33**, 1817 (2000).
- ⁷N. Bozinovic *et al.*, "Terabit-scale orbital angular momentum mode division multiplexing in fibers," *Science* **340**, 1545–1548 (2013).
- ⁸A. Mair, A. Vaziri, G. Weihs, and A. Zeilinger, "Entanglement of the orbital angular momentum states of photons," *Nature* **412**, 313–316 (2001).
- ⁹D. Naidoo *et al.*, "Controlled generation of higher-order Poincaré sphere beams from a laser," *Nat. Photonics* **10**(5), 327 (2016).
- ¹⁰J. F. Bisson *et al.*, "Radially polarized ring and arc beams of a neodymium laser with an intra-cavity axicon," *Opt. Express* **14**(8), 3304–3311 (2006).
- ¹¹L. Marrucci, C. Manzo, and D. Paparo, "Optical spin-to-orbital angular momentum conversion in inhomogeneous anisotropic media," *Phys. Rev. Lett.* **96**(16), 163905 (2006).
- ¹²N. Radwell *et al.*, "Achromatic vector vortex beams from a glass cone," *Nat. Commun.* **7**, 10564 (2016).
- ¹³K. Dholakia *et al.*, "Second-harmonic generation and the orbital angular momentum of light," *Phys. Rev. A* **54**(5), R3742 (1996).
- ¹⁴G. Walker, A. S. Arnold, and S. Franke-Arnold, "Trans-spectral orbital angular momentum transfer via four-wave mixing in Rb vapor," *Phys. Rev. Lett.* **108**(24), 243601 (2012).
- ¹⁵G. Prabhakar *et al.*, "Octave-wide supercontinuum generation of light-carrying orbital angular momentum," *Opt. Express* **27**(8), 11547–11556 (2019).
- ¹⁶R. J. Essiambre *et al.*, "Experimental investigation of inter-modal four-wave mixing in few-mode fibers," *IEEE Photonics Technol. Lett.* **25**(6), 539–542 (2013).
- ¹⁷F. Parmigiani *et al.*, "All-optical mode and wavelength converter based on parametric processes in a three-mode fiber," *Opt. Express* **25**(26), 33602–33609 (2017).
- ¹⁸J. Demas *et al.*, "Intermodal nonlinear mixing with Bessel beams in optical fiber," *Optica* **2**(1), 14–17 (2015).
- ¹⁹J. Hansryd *et al.*, "Fiber-based optical parametric amplifiers and their applications," *IEEE J. Sel. Top. Quantum Electron.* **8**(3), 506–520 (2002).
- ²⁰J. Demas *et al.*, "Wavelength-agile high-power sources via four-wave mixing in higher-order fiber modes," *Opt. Express* **25**(7), 7455–7464 (2017).
- ²¹S. Ramachandran and P. Kristensen, "Optical vortices in fiber," *Nanophotonics* **2**(5–6), 455–474 (2013).
- ²²G. P. Agrawal, "Nonlinear fiber optics," in *Nonlinear Science at the Dawn of the 21st Century* (Springer, Berlin, Heidelberg, 2000), pp. 195–211.
- ²³P. Gregg, P. Kristensen, and S. Ramachandran, "Conservation of orbital angular momentum in air-core optical fibers," *Optica* **2**(3), 267–270 (2015).
- ²⁴P. Vaity, J. Banerji, and R. P. Singh, "Measuring the topological charge of an optical vortex by using a tilted convex lens," *Phys. Lett. A* **377**(15), 1154–1156 (2013).
- ²⁵N. Bozinovic *et al.*, "Control of orbital angular momentum of light with optical fibers," *Opt. Lett.* **37**(13), 2451–2453 (2012).
- ²⁶K. Rottwitt *et al.*, "Inter-modal Raman amplification of OAM modes," *APL Photonics* **4**(3), 030802 (2019).
- ²⁷J. E. Sharping *et al.*, "Octave-spanning, high-power microstructure-fiber-based optical parametric oscillators," *Opt. Express* **15**(4), 1474–1479 (2007).